Structural, Optical and Cytotoxic Analysis of Sr-Doped CuS Nanoparticles for Lung Cancer Applications

Asma'a Ahmed AL-Adhreai[1,2], A.M. Abdulwahab[2]* and A. H. Al-Hammadi[1]

[1]Department of Physics, Faculty of Sciences, Sana'a University, Sana'a, Yemen,
[2]Department of Physics, Faculty of Applied Sciences, Dhamar University, Dhamar, Yemen

*Corresponding author: abduhabdulwahab@yahoo.com

ABSTRACT

Copper sulfide (CuS) nanoparticles have garnered significant interest due to their unique structural, optical, and biological properties, making them promising candidates for cancer therapy. This work systematically examines how strontium incorporation influences the structural properties, optical behavior, and anticancer activity of copper sulfide nanoparticles for potential lung cancer therapeutics. Using the co-precipitation approach, Sr-doped CuS nanoparticles with different Sr concentrations were produced. Characterization techniques, including XRD, TEM, and UV-VIS-NIR spectroscopy, were employed to analyze their physicochemical properties. The results indicate that Sr doping enhances crystallinity, modifies the bandgap, and influences optical conductivity. Cytotoxicity analysis using MTT assays on A549 lung cancer cells demonstrated that Sr-doped CuS nanoparticles exhibit enhanced anticancer activity compared to pure CuS. The 2.5% Sr-doped sample showed the most significant reduction in cell viability. These findings suggest that Sr-doped CuS nanoparticles are promising candidates for biomedical applications. However, further studies are needed to assess their photothermal and photodynamic effects under controlled light exposure.

ARTICLE INFO

1. INTRODUCTION

CuS nanoparticles have garnered considerable research attention owing to their distinctive physicochemical characteristics and versatile applications in diverse domains, such as optoelectronics, photocatalysis, and biomedical technologies. These nanoparticles exhibit p-type semiconductor behavior, with low resistivity, high absorption coefficients, and excellent charge transport properties [1]. Their low cytotoxicity and cost-effectiveness further enhance their potential for biomedical applications [2]. Among the various modification strategies, controlled elemental doping has emerged as a powerful approach to tailor the properties of semiconductor nanomaterials for specific applications [3]. In biomedical applications, CuS nanoparticles show promise for cancer therapy because of their strong NIR absorption and photothermal conversion capabilities [4]. This potential is especially relevant for lung cancer treatment, where current

therapies face challenges including late detection, tumor heterogeneity, and treatment resistance [5, 6].

Strontium (Sr) has been successfully employed as a dopant to modify the properties of various semiconductors including $BiFeO_3$, CdS, and ZnO for numerous applications [7]. However, despite the biological compatibility of Sr^{2+} and its ability to modulate cellular responses [8–10], its specific effects on CuS nanoparticles remain unexplored.. This study hypothesizes that Sr^{2+} doping will (1) improve CuS crystallinity through ionic size matching, (2) tune the optical properties for optical applications, and (3) increase selective cytotoxicity against lung cancer cells. We tested these hypotheses through the systematic synthesis of Sr-doped CuS nanoparticles via co-precipitation, followed by comprehensive characterization of their structural (XRD, TEM), optical (UV-VIS-NIR), and biological (MTT assays) properties. Our work provides the first demonstration of

the Sr^{2+} doping simultaneously optimization of the physical properties and anti-cancer activity of CuS nanoparticles against human lung cancer cells.

2. EXPERIMENTAL TECHNIQUES

2.1. MATERIALS

The materials used for synthesizing the nanoparticles included sodium sulfide hydrate (Na_2S, HIMEDIA, $\geq 65\%$), strontium chloride hexahydrate ($SrC_{l2} \cdot 6H_2O$, Fluka, $\geq 97\%$), and copper chloride dihydrate ($CuC_{l2} \cdot 2H_2O$, Sigma Aldrich, $\geq \%99$). Analytical -grade reagents were employed without further purification, and distilled water was used as the reaction medium.

2.2. SAMPLE PREPARATION

A co-precipitation method was employed to create $Cu_{1-x}Sr_xS$ nanoparticles with varying compositions ($x = 0.00, 0.025, 0.05, 0.075,$ and 0.1). Copper chloride and strontium chloride, each at a concentration of 2 M, were combined in distilled water to form a green solution. Concurrently, a 2 M sodium sulfide hydrate solution was prepared. The precursor solution was treated by dropwise addition of aqueous sodium sulfide under continuous stirring (1 h, 25°C), after which the reaction mixture was aged for two hours. No external pH adjustment was applied during synthesis, and the reaction proceeded at the natural pH of the solution. The synthesized precipitate was vacuum-filtered, purified via sequential solvent washing (deionized water $\rightarrow$ ethanol), dried at 100°C, and ground for characterization. Fig. 1 shows a clear flowchart of the production of Sr-doped CuS nanoparticles.
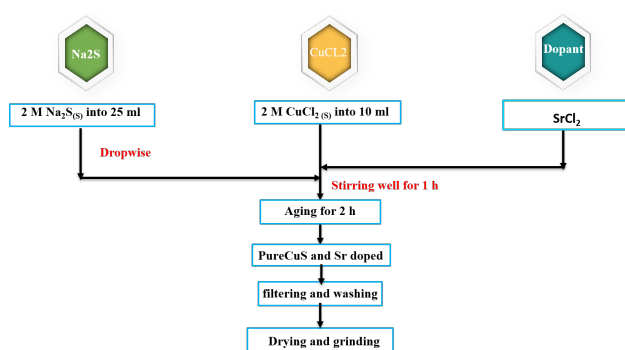

Figure 1. Flowchart of the production of pure and Sr-doped CuS NPs

2.3. CHARACTERIZATION

The synthesized CuS nanoparticles were characterized using several analytical techniques. X-ray diffraction (XRD) patterns were recorded using an XD-2 X-ray diffractometer equipped with CuK_α radiation ($\lambda = 1.54$ Å), operating at 36 kV and 20 mA. Elemental analysis was performed via TXRF (XRF, S8 TIGER, Germany) at the Yemeni Geological Survey and Minerals Resources Board to quantify the sample compositions. High-resolution transmission electron microscopy at high resolution (HR-TEM) was performed with a field-emission JEOL JEM-2100 system, followed by digital image analysis using ImageJ. For optical property analysis, UV–VIS–NIR spectra were obtained in the diffuse reflectance mode, using a JASCO V-570 spectrophotometer equipped with an integrating sphere.

2.4. CELL LINE

The A549 human lung adenocarcinoma cells were obtained from the American Type Culture Collection (ATCC) and maintained in Dulbecco's Modified Eagle's medium (DMEM) supplemented with 10% fetal bovine serum (FBS), 100 U/mL penicillin, and 0.1 mg/mL streptomycin. The cells were then incubated at 37°C in a humidified incubator with 5% CO_2.

2.5. IN VITRO CYTOTOXICITY

Cell viability of A549 cells was determined using the MTT assay, which is a widely used colorimetric method for quantifying viable cells. The principle involves reduction of the yellow tetrazolium salt (3-(4,5-dimethylthiazol-2-yl)-2,5-diphenyltetrazolium bromide) by mitochondrial dehydrogenases in metabolically active cells, producing insoluble purple formazan crystals. These crystals were then dissolved using dimethyl sulfoxide (DMSO) to, yielding a colored solution. The absorbance of this solution was measured between 500 and 600 nm, and the reduction in absorbance correlated with the percentage of cell inhibition [11].

After culturing for 24 h at a density of $2-2.5 \times 10^4$ cells/well in a 96-well tissue culture plate with 180 μL of complete growth medium per well, the cells were treated with 20 μL of the test item. The drug stock solutions were prepared using DMSO. All compounds were synthesized at eight different concentrations (300, 100, 30, 10, 3, 1, 0.3, and 0.1 μg/ml) in the growth medium. The cells were then treated for 72 h.

Next, a newly prepared MTT salt (5 mg/ml; Sigma) was added to each well. An equivalent volume of 200 μL DMSO was added to each well after the MTT solution was carefully removed, and the wells were shaken for 60 min. Cell proliferation was quantified by measuring absorbance at 590 nm using a Thermo Scientific Multiskan® EX microplate reader (USA). The experiment was conducted in duplicate. Nonlinear fitting of the dose-response curve and GraphPad Prism (8) were used to determine the IC_{50} values. DMSO (0.01%) was used as a vehicle-only control in the MTT assay. The results are reported as the mean $\pm$ SD of three independent experiments, each performed in triplicate. All cell treatments and MTT assays were conducted under standard cell -culture conditions and ambient laboratory lighting. No external light or NIR irradiation was applied during the

72-h treatment period or subsequent viability measurements, ensuring that the observed cytotoxicity reflects the nanoparticles' inherent effects rather than light-activated mechanisms. The MTT assay and IC$_{50}$ analysis were performed by an external laboratory in Egypt. Although GraphPad Prism (8) was used to fit IC$_{50}$ curves, complete statistical analysis outputs such as ANOVA tables and post-hoc test results were not available due to the outsourcing of cytotoxicity testing. This is acknowledged as a limitation of this study.

3. RESULTS AND DISCUSSION

3.1. STRUCTURAL PROPERTIES

X-ray diffraction (XRD) patterns of Sr-doped CuS nanoparticles with different Sr concentrations (2.5, 5, 7.5, and 10%) and pure CuS nanoparticles are shown in Fig. 2. The prominent peaks are indexed with Miller indices (e.g., 101, 102, 006, 110), which confirm the presence of a CuS crystalline structure with a hexagonal phase. These findings matched the standard hexagonal covellite CuS pattern (JCPDS 06-0464). A minor peak labeled as "#" appears in some Sr-doped samples at about 2θ =25.5°, this angle

corresponded to the JCPDS card number 08-0489 for SrS. This suggests that at higher concentrations, some Sr atoms may not fully integrate into the CuS lattice and instead form a separate SrS phase. The pure CuS sample shows well-defined peaks without the SrS, confirming the purity of the sample. These peaks align closely across all samples, indicating that the introduction of Sr does not significantly alter the fundamental CuS crystalline structure. However, slight shifts in peak positions may reflect lattice changes due to Sr incorporation [12].

The intensities of the peaks decreased slightly with increasing Sr doping. This could suggest a decrease in crystallinity or an increase in defects as more Sr was incorporated. Reduced crystallinity often results in a lower peak intensity. As Sr doping increases, the slight shifts and intensity changes suggest that Sr was successfully doped into the CuS lattice [13]. By using Scherrer's formula (Eq. 1), the crystallite sizes of the produced samples were determined [14]:

$$D = \frac{0.9\lambda}{\beta \, \text{CoS} \, \theta} \qquad (1)$$

Where D is the= crystallite size (nm), β is the Peak width at half-maximum intensity, λ 0.154 nm (characteristic X-ray), and θ is the Angle (°degree).

The crystallite sizes of the samples are listed in Table 1. As can be seen, the crystallite size remained relatively close to the value for the undoped sample, with only slight increases or decreases across different doping levels. At 7.5% Sr doping, the crystallite size reaches a peak value (16.04 nm), suggesting that this concentration may allow Sr ions to better integrate into the CuS lattice, possibly causing a slight lattice expansion. For 10% Sr, the crystallite size slightly decreased again, which may indicate the formation of Sr-related defects or strain in the lattice as more Sr
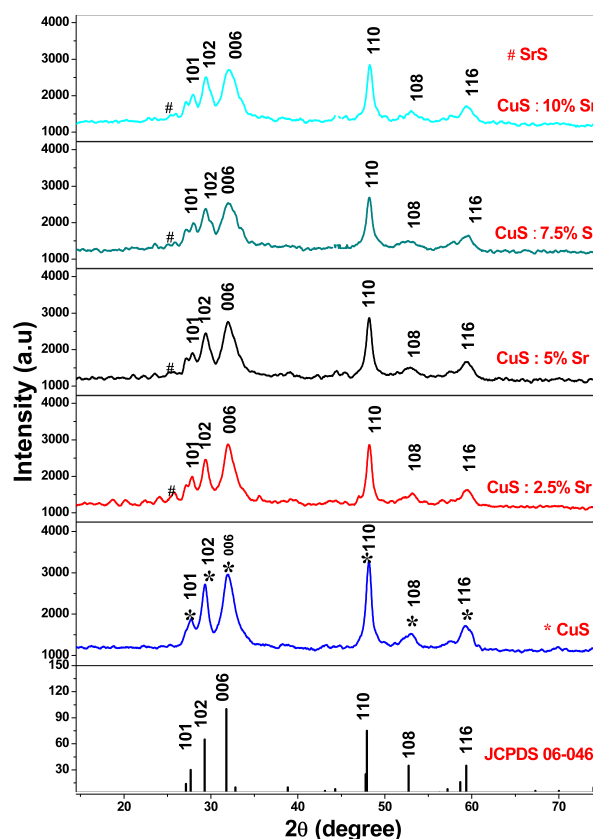

Figure 2. XRD patterns of pure and Sr-doped CuS nanoparticles. Peaks are indexed according to hexagonal covellite CuS (JCPDS 06-0464).

atoms entered the structure. Doping often introduces strain or imperfections, which can cause minor changes in the crystallite size. Here, the limited changes in crystallite size imply that low- to- moderate levels of Sr doping can be achieved without significantly disrupting the CuS lattice.

The lattice parameters a and c provide valuable information about the structural modifications induced by Sr doping in the CuS nanoparticles. For a hexagonal-phase structure, the lattice parameters a, b, and c were computed from the dominant (hkl) diffraction peak for all prepared specimens using the following relationship [15]:

$$\frac{1}{d^2} = \frac{4}{3}\left[\frac{h^2 + hk + k^2}{a^2}\right] + \frac{l^2}{c^2} \qquad (2)$$

The obtained values are listed in Table 1. The value slightly decreases as Sr doping increases, reaching its lowest value at 10% Sr doping (16.22 Å). Sr^{2+} (ionic radius = 1.18 Å) is larger than Cu^{2+} (0.73 Å) [16], so Sr incorporation would typically expand the lattice. However, the observed decrease in "a" suggests that Sr atoms replaced Cu sites while introducing internal strain, which led to lattice contraction rather than expansion. This could be due to Sr^{2+} the forming of stronger bonds with S^{2-} compared to Cu^{2+}, pulling the surrounding atoms closer and decreasing the lattice spacing. The lattice contraction rather than expan-

sion agrees with published papers for other materials, such as Sr⁻ doped ZnO [17]. The c value remained relatively stable across the different Sr doping levels, fluctuating only slightly. Because Sr replaces Cu primarily within the same crystallographic plane, the c-axis remains mostly unchanged. Any slight variation in c could be due to local strain effects rather than significant structural reorganization.

Table 1. Crystallographic characteristics of prepared samples including crystallite size, 2θ values, FWHM, and lattice parameters.

The prepared samples	D(nm)	2θ (degree)	FWHM (degree)	Lattice constant	
				a (Å)	c (Å)
Pure	15.15	48.39	0.575	16.37	3.7552
Sr: CuS(2.5%)	15.67	48.46	0.556	16.25	3.7552
Sr: CuS(5%)	15.15	48.42	0.575	16.38	3.7538
Sr: CuS(7.5%)	16.04	48.45	0.543	16.29	3.7566
Sr: CuS(10%)	15.39	48.46	0.566	16.22	3.7538

3.2. TOTAL REFLECTION X-RAY FLUORESCENCE

Total Reflection X-ray Fluorescence (TXRF) spectroscopy was employed to verify the incorporation of dopants into the synthesized samples. The analysis confirmed the successful integration of Sr in all the doped specimens, as evidenced by the characteristic Sr emission peaks. The quantitative elemental composition data for Cu, sulfur, and Sr are presented in Table 2.

Table 2. TXRF-derived elemental concentrations in pristine and Sr-doped CuS nanoparticles

Samples	Pure	2.5% Sr	5% Sr	7.5% Sr	10% Sr
Cu, %	55.25	52.61	46.89	47.02	48.05
S, %	44.39	45.51	46.48	45.31	45.15
Sr, %	-	1.51	6.24	7.33	6.45
Cl, P, Ca (traces), %	0.36	0.37	0.39	0.34	0.35

3.3. TEM ANALYSIS

The TEM images and the particle size distribution histograms of the prepared nanoparticles are shown Fig. 3. and Fig. 4 provide valuable insights into the morphology and size of the prepared nanoparticles: for pure CuS, the particle sizes are with an average close to 16.67 nm. The nanoparticles exhibited irregular, aggregated structures, and their morphology suggested the absence of doping-induced strain or anisotropy.

For 2.5% Sr-doped CuS, the particle sizes was 16.27 nm. The smaller dimensions compared to those of pure CuS suggest that low-level Sr doping might reduce particle growth, likely due to the slight lattice strain.

The particles remained aggregated but showed slightly improved dispersion compared to that of the pure sample. For the 5% Sr-doped CuS, the particle size was 16.20 nm, indicating a further reduction in size with increased Sr doping. The improved dispersion was visible, although some aggregation remained. The morphology shows evidence of strain-induced modifications.

The 7.5% Sr-doped CuS particles were elongated and exhibited a rod-like structure. The sizes are more variable, with dimension of 17.32 nm. The measured aspect ratios of 7.5% Sr-doped CuS revealed an average of 3.33 ± 0.99, confirming the anisotropic (rod-like) nature of the particles at this doping level. This suggests anisotropic growth due to doping-induced strain, which is consistent with the changes observed in the XRD and optical properties.

For 10% Sr-doped CuS, the particle size wais 16.46 nm, showing a slight decrease compared to that of 7.5% Sr-doped CuS. Aggregation is more pronounced, possibly because of an increase in surface energy [18].

3.4. OPTICAL PROPERTIES

3.4.1. The diffuse reflectance

The diffuse reflectance spectra of pure and Sr-doped CuS nanoparticles are shown in Fig. 5. The reflectance (R) decreased gradually with increasing wavelength (400–800 nm), indicating enhanced light absorption in the visible to near-infrared (NIR) range. This trend is consistent with the semiconducting nature of CuS, which exhibits strong absorption owing to its narrow bandgap. The reflectance values systematically increased at higher Sr doping concentrations in the CuS nanoparticles, demonstrating a clear doping-dependent optical response.

3.4.2. Band gap energy (E_g)

The Kubelka–Munk function $F(R) = \frac{(1-R)^2}{2R}$ was employed to convert reflectance (R) into absorption-equivalent values, which is mathematically proportional to the absorption coefficient (α) for scattering-dominant samples. The Tauc equation was used to estimate the band gap energy (E_g) [19]:
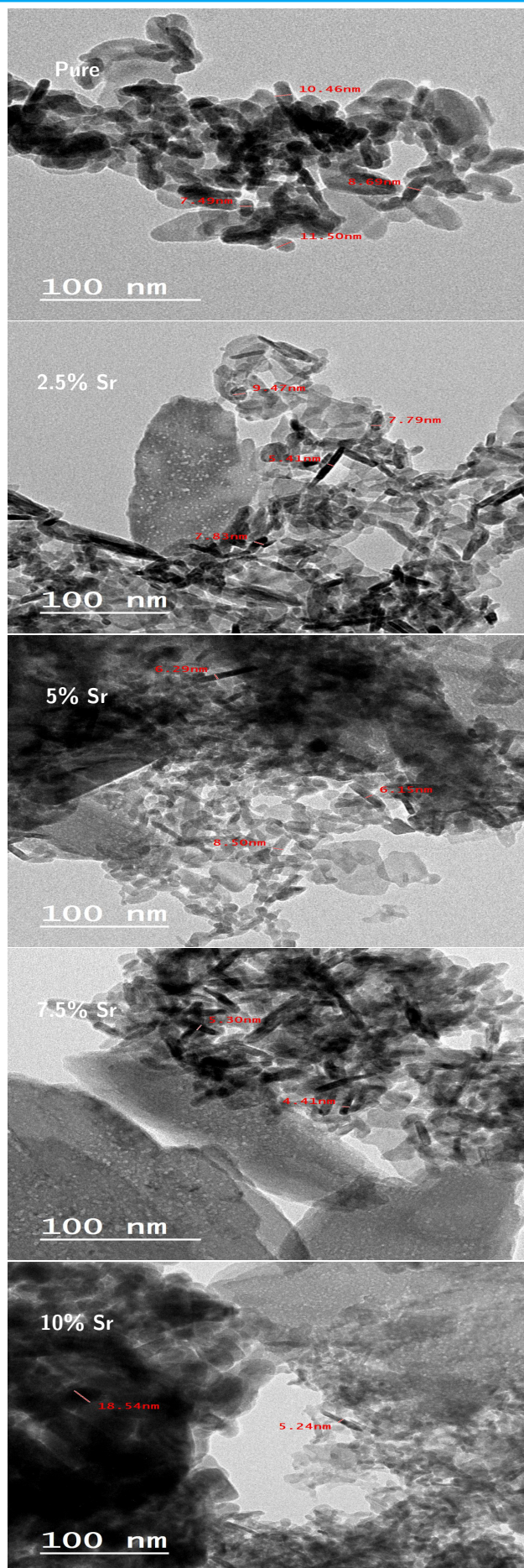
Figure 3. TEM images of pure and Sr-doped CuS nanoparticles. Each image includes a scale bar of 100 nm.
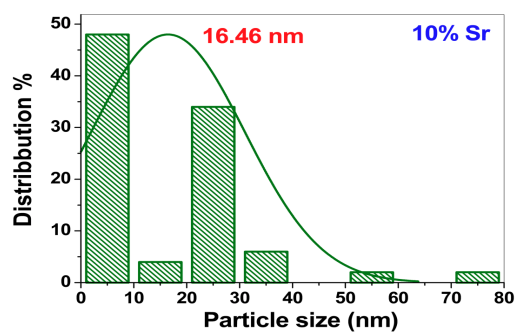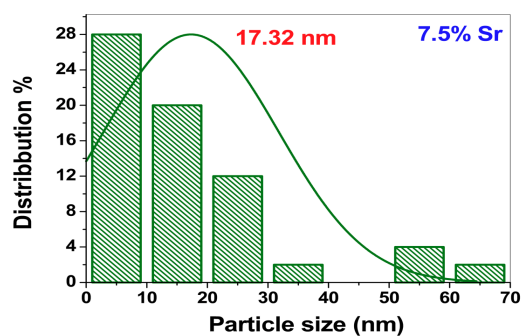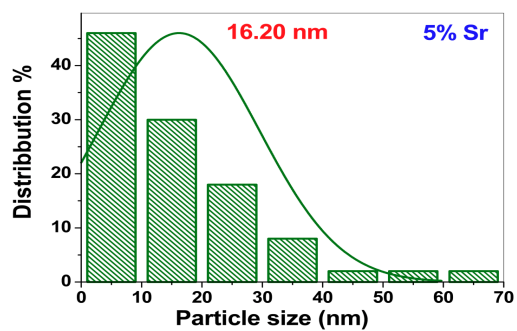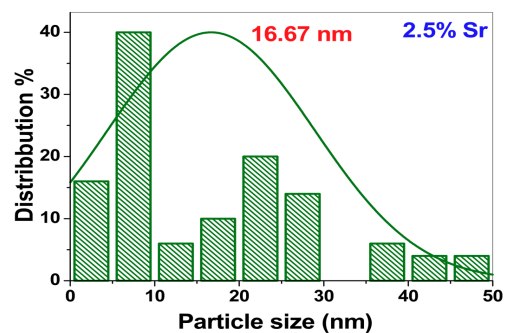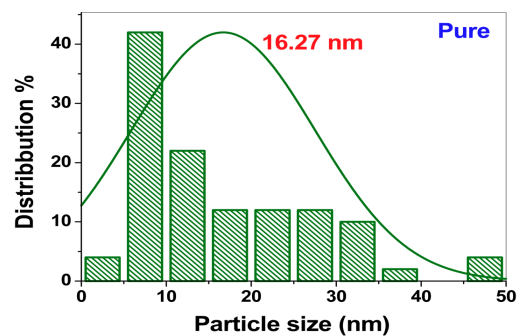

Figure 4. Particle size distribution histograms for pure and Sr-doped CuS nanoparticles measured from TEM images using ImageJ.
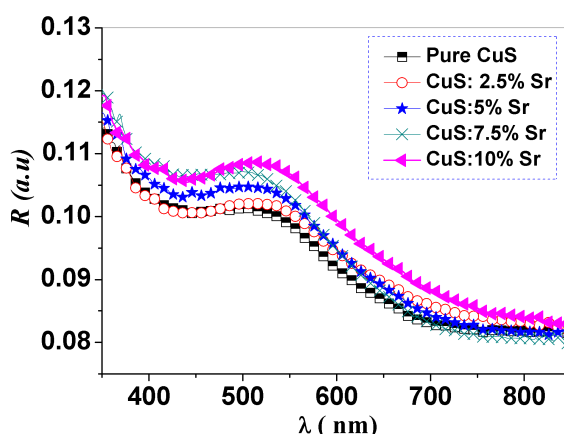
Figure 5. UV–VIS–NIR diffuse reflectance spectra (R) of pure and Sr-doped CuS nanoparticles with different Sr doping concentrations (2.5%, 5%, 7.5%, and 10%).

Figure 6. Tauc plots of $(F(R)E)^2$ versus photon energy (eV) for pure and Sr-doped CuS nanoparticles used to determine bandgap energies

$$(F(R)E) = A\,(E - E_g)^n \qquad (3)$$

$F(R)$ represents the absorption coefficient α; for the permitted direct transition, n equals 1/2, E_g is the band gap energy of CuS, B is a constant, and E is the input photon energy. Extrapolating the linear part of $(\alpha E)^2$ against E plots to the x-axis yields an energy gap.

Fig. 6 shows the optical bandgap (E_g) of the prepared nanoparticles, calculated using Tauc's plot $(F(R)E)^2$ versus photon energy (E). The measured bandgaps of the prepared nanoparticles are listed in Table 3.

As can be seen, pure CuS has a bandgap of 1.38 eV. For 2.5% Sr, the bandgap increases to 1.43 eV, indicating a slight modification of the electronic structure, likely due to the incorporation of Sr ions into the CuS lattice. For 5% Sr, the bandgap further increases to 1.50 eV. This consistent increase suggests enhanced electron localization caused by the introduction of Sr, which affects the density of states in the conduction, and valence bands, respectively). The 7.5% Sr bandgap decreased slightly to 1.44 eV. The observed deviation may result from the electronic transition, which is most pronounced in the 7.5%- doped sample because this level is optimal for enhanced transitions [16]. 10% Sr, the bandgap reaches 1.59 eV.

A significant increase was observed, suggesting the saturation of Sr in the CuS lattice, altering its band structure. The findings show that doped CuS exhibits a wider band gap than pure CuS, as the introduction of dopants supplies free electrons, causing the Fermi level to shift toward the conduction band [20]. Comparing the pure CuS NPs to the bulk CuS (E_g = 1.85 eV), the undoped sample had a narrow E_g value of 1.38 eV [21]. The reported band gap values for CuS nanoparticles vary across studies, with Aziz *et al.* [22] measuring approximately 1.29 eV, Saranya *et al.* [23]reporting 1.64 eV, and Pal *et al.* [24] reported a bandgap o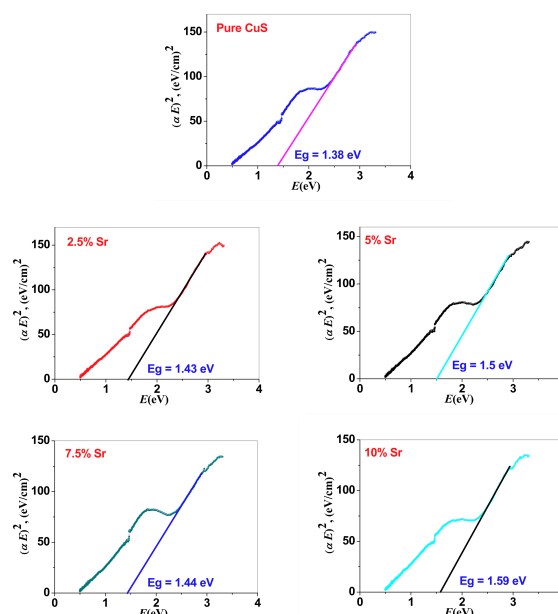f 1.09 eV. These findings suggest that Sr doping is a viable method for tuning the optical properties of CuS nanoparticles, with potential implications for their application in optoelectronic devices.

3.4.3. Optical conductivity (σ_{opt})

Because the optical conductivity in semiconductors is highly dependent on the optical band gap, it is essential to investigate σ_{opt} in this study. Good optical conductivity is a basic property for the fabrication of LED and optoelectronic devices [25]. Several factors influence the optical conductivity of the synthesized nanoparticles, including the absorption coefficient, extinction coefficient, refractive index, and incident photon frequency [26]. Optical conductivity was derived from the transformed absorption data, where $F(R) = \alpha$. The following equation can be used to compute the optical conductivity [27]:

$$\sigma_{opt} = \frac{\alpha n c}{4\pi} \qquad (4)$$

Where c denotes the electromagnetic wave propagation speed in free space. The comparative optical conductivity behaviors of the pure and Sr-incorporated CuS nanomaterials are shown in Fig. 7. It is noteworthy that σ_{opt} initially exhibited a steeper decrease with an increasing E, followed by an increase, and finally a tendency to decrease again.

As evident from Fig. 7, the undoped CuS sample exhibits maximum optical conductivity (σ_{opt} = 2.24 × 10^{10} S^{-1}), which progressively decreases to 2.17 × 10^{10}S^{-1} with increasing Sr doping concentration up to 10%. The observed reduction in optical conductivity with higher Sr doping correlates directly with bandgap broadening, as fewer charge carriers become available for conduction in wider-bandgap materials. This inverse correlation underscores the suitability
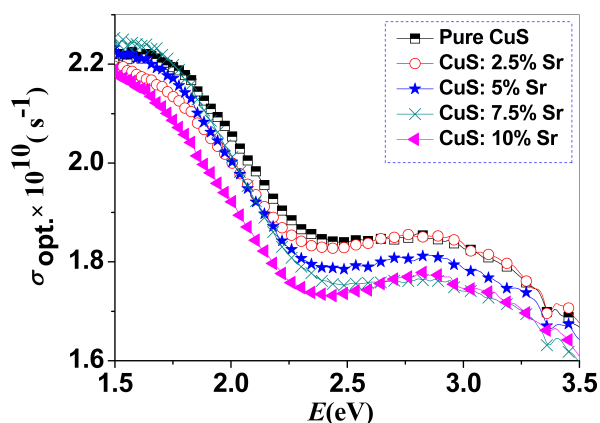
Figure 7. Optical conductivity spectra of pure and Sr-doped CuS nanoparticles as a function of photon energy. Conductivity is calculated from a transformed absorption data.

of the material for optoelectronic and photovoltaic applications, where precise modulation of electronic and optical characteristics is critical [28].

3.4.4. The refractive index dispersion

The refractive index dispersion of both pure and Sr-doped CuS nanoparticles follows the Wemple–DiDomenico single-oscillator model, allowing the determination of the dispersion energy parameters. A well-defined correlation exists between the refractive index and photon energy (E), expressed mathematically as [29]:

$$n^2 - 1 = \frac{E_d E_O}{\left(E_O^2 - E^2\right)} \tag{5}$$

Here, E_o (oscillator energy) and E_d (dispersion energy, quantifying optical transition strength) are material constants, with n being the refractive index and E the photon energy. The refractive index was determined from reflectance data using the relation $n = (1 + \sqrt{R})/(1 - \sqrt{R})$, derived from Fresnel's equations for normal incidence [30]. The derived dispersion parameters are essential for establishing universal empirical relationships across various semiconductor materials, where dispersion is regarded as having a significant influence in selecting the optical material because it plays a critical role in the development of spectral dispersion devices and photonic communication systems [31].

Fig. 8 shows the plots of $1/(n^2\text{-}1)$ vs. $(E)^2$ for all the synthesized CuS samples. By fitting the data in these plots to straight lines and from the intercepts E_o/E_d and slopes $(E_o\ E_d)^{-1}$, E_o and E_d were determined.

Table 3 presents the calculated optical constants E_o and E_d, revealing the maximum values for both parameters at a concentration of 2.5, suggesting an optimal doping level for enhanced optical performance.
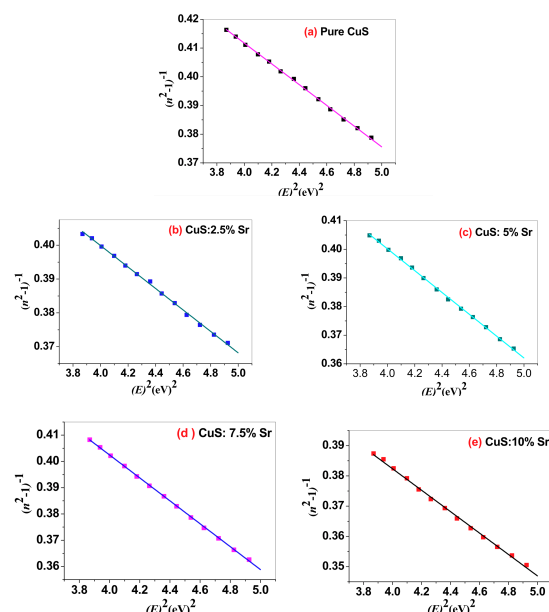

Figure 8. Plots of $1/(n^21)$ versus E^2 for determining the dispersion parameters E_o and E_d using the Wemple–DiDomenico model.

Table 3. E_g, E_d and E_o of prepared nanoparticles.

Nanomaterial	Eg (eV)	E_o (eV)	E_d (eV)
Pure	1.38	3.92	7.05
2.5% Sr	1.43	4.11	7.80
5% Sr	1.50	3.80	6.88
7.5% Sr	1.44	3.63	6.30
10% Sr	1.59	3.84	7.34

3.5. EFFECT OF DOPING ON THE CYTOTOXICITY OF CuS NPs TOWARD HUMAN LUNG CANCER CELLS

Before use in humans, new drugs and compounds must be examined for their toxicological profiles. As concerns have been raised about the possible risk of employing NPs in medicinal applications, measuring the IC_{50} of NPs helps researchers evaluate the potential harmful effects associated with their persistent accumulation in organs [32]. IC_{50} values were derived from dose-response curves, representing the drug concentration at which tumor cell growth was inhibited by 50% compared to untreated cultures [33].

The existing literature provides limited investigation into the cytotoxic potential of synthetically produced CuS nanoparticles against pulmonary carcinoma cell lines. Table 4 presents the IC_{50} values obtained from the MTT cytotoxicity testing of the prepared compounds against human lung cancer (A549) cell lines. All tested samples were compared to doxorubicin, a clinically established anticancer drug, for cytotoxicity evaluation. Fig. 9 displayed the cell viability data (obtained by the MTT experiment) versus the logarithm of the concentration and IC_{50} values obtained for the
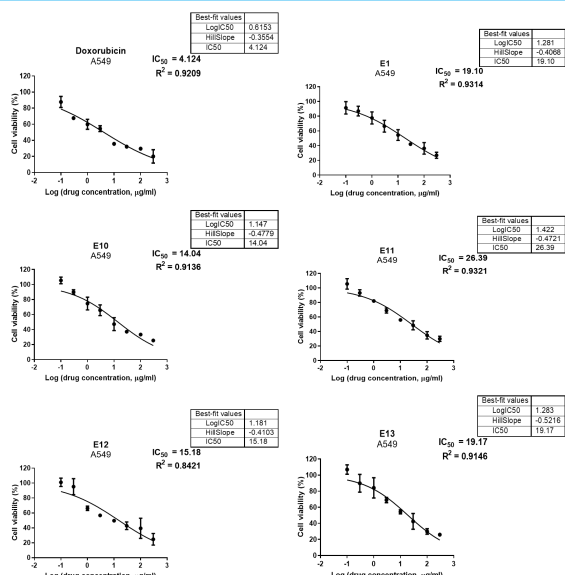
Figure 9. Plot of cell viability percentage against the logarithm of compound concentration, including IC$_{50}$ values calculated for the tested samples.

prepared samples as well as doxorubicin.

The MTT assay results shown in Table 4 and Fig. 10 indicate that all test samples had a pronounced cytotoxic effect on A549 cells compared to doxorubicin. Cell death caused by Sr-CuS NPs was higher than that caused by pure CuS NPs, except for the 5 and 10% doped samples. Although the 2.5% Sr–CuS sample demonstrated the highest cytotoxicity (lowest IC$_{50}$), the trend did not correlate linearly with the doping concentration. The reduction in cytotoxic effects at 5% and 10% Sr may be due to changes in aggregation behavior or cellular uptake, potentially reducing the effective intracellular concentration [34]. However, these possibilities were not directly evaluated in the current study and will be investigated in future studies through aggregation and uptake assays. The enhanced cytotoxicity of Sr-doped CuS NPs (except at 5-10% doping) suggests that doping influences nanoparticle-biological interactions, although the precise mechanisms require further study. Future work should include photothermal conversion efficiency, ROS measurement, apoptosis assays, and nanoparticle uptake quantification to elucidate these mechanisms.

We recognize that the evaluation of nanoparticle toxicity in normal cells is essential for determining a therapeutic index. Future studies will include cytotoxicity assays on a normal lung epithelial cell line (e.g., BEAS-2B) to calculate the selectivity index and further validate the safety profile of Sr-doped CuS nanoparticles.

4. CONCLUSION

This study demonstrates that Sr doping effectively enhances the structural, and optical properties, and anticancer activity of CuS nanoparticles. XRD, TXRF, and TEM analyses confirmed the successful integration of Sr into the CuS lattice,

Table 4. In comparison to doxorubicin, the cytotoxic activity of prepared nanoparticles toward human lung cancer cells.

Tested samples	IC$_{50}$ (μg/ml)$^{(*)}$ mean $\pm$ SD
Doxorubicin	4.12 $\pm$ 0.35
Pure	19.10 $\pm$ 2.16
2.5% Sr	14.04 $\pm$ 0.59
5% Sr	26.39 $\pm$ 3.18
7.5% Sr	15.18 $\pm$ 3.89
10% Sr	19.17 $\pm$ 2.11

(*) IC$_{50}$ ranges: 1–10 μg/mL (extremely strong), 11–20 μg/mL (strong), 21–50 μg/mL (moderate), 51–100 μg/mL (weak), and >100 μg/mL (non-cytotoxic) [35].
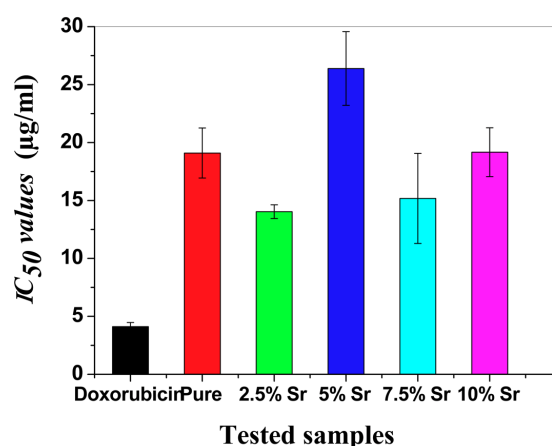

Figure 10. IC$_{50}$ values of pure and Sr-doped CuS nanoparticles against A549 cells (mean $\pm$ SD, n = 3).

leading to a modified crystallinity and bandgap energy. Optical studies revealed that Sr doping influences the bandgap widening and optical conductivity. Furthermore, cytotoxicity assessments indicated that Sr-doped CuS nanoparticles exhibited higher anticancer activity against A549 lung cancer cells, particularly at lower Sr concentrations. These in vitro findings suggest that Sr-doped CuS nanoparticles warrant further investigation as potential candidates for lung cancer treatment, pending future validation through in vivo studies and comprehensive safety assessments.

REFERENCES

[1] H. Escobar-Sánchez, C. C. Pardo, N. Benito, *et al.*, "Plasmonic and photothermal effects of cus nanoparticles biosynthesized from acid mine drainage with potential drug delivery applications," Int. J. Mol. Sci. **24**, 16489 (2023).

[2] X. Zhu, Y. Zhang, H. Huang, *et al.*, "Folic acid-modified and functionalized cus nanocrystal-based nanoparticles for combined tumor chemo-and photothermal therapy," J. Drug Target. **25**, 425–435 (2017).

[3] X. Peng, F. Ai, L. Yan, *et al.*, "Synthesis strategies and biomedical applications for doped inorganic semiconductor nanocrystals," Cell Reports Phys. Sci. **2**, 100436 (2021).

[4] L. Li, L. Rashidi, M. Yao, *et al.*, "Cus nanoagents for photodynamic and photothermal therapies: Phenomena and possible mechanisms," Photodiagnosis Photodyn. Ther. **19**, 5–14 (2017).

[5] F. Bray, J. Ferlay, I. Soerjomataram, *et al.*, "Global cancer statistics 2018: Globocan estimates of incidence and mortality worldwide for 36 cancers in 185 countries," CA: A Cancer J. for Clin. **68**, 394–424 (2018).

[6] R. Herbst, D. Morgensztern, and C. Boshoff, "The biology and management of non-small cell lung cancer," Nature **553**, 446–454 (2018).

[7] M. Shkir, A. Khan, M. Hamdy, and S. AlFaify, "A facile microwave synthesis of pbs: Sr nanoparticles and their key structural, morphological, optical, photoluminescence, dielectric and electrical studies for optoelectronics," Mater. Res. Express **6**, 1250e6 (2020).

[8] I. Ifijen, M. Maliki, I. Odiachi, *et al.*, "Performance of metallic-based nanomaterials doped with strontium in biomedical and supercapacitor electrodes: a review," Biomed. Mater. & Devices **1**, 402–418 (2023).

[9] S. Mukherjee and M. Mishra, "Application of strontium-based nanoparticles in medicine and environmental sciences," Nanotechnol. for Environ. Eng. **6**, 25 (2021).

[10] M. Taeby, M. Ashoub, M. Asghari, *et al.*, "Sol–gel synthesis of strontium ferrate (srfeo_3) nanoparticles and evaluation of anti-leukemic effects against leukemic cell lines," J. Sol-Gel Sci. Technol. **109**, 56–65 (2024).

[11] H. Fahmy, N. Ebrahim, and M. Gaber, "In-vitro evaluation of copper/copper oxide nanoparticles cytotoxicity and genotoxicity in normal and cancer lung cell lines," J. Trace Elem. Med. Biol. **60**, 126481 (2020).

[12] R. Zeinodin, F. Jamali-Sheini, and M. Cheraghizade, "Physical properties of pb-doped cus nanostructures for optoelectronic applications," Mater. Sci. Semicond. Process. **123**, 105501 (2021).

[13] E. Hastuti, A. Subhan, P. Amonpattaratkit, *et al.*, "The effects of fe-doping on mno2: Phase transitions, defect structures and its influence on electrical properties," RSC Adv. **11**, 7808–7823 (2021).

[14] A. Al-Hammadi, A. Al-Sharabi, and A. Alnehia, "Green and chemically prepared zinc sulfide nanoparticles: a comparative study," Sana'a Univ. J. Appl. Sci. Technol. **1** (2023).

[15] S. Khoreem and A. h. Al-Hammadi, "Structural, spectral and electrical properties of bani2-xznxfe16o27 nanoparticles ferrites," Sana'a Univ. J. Appl. Sci. Technol. **1** (2023).

[16] A. Al-Hammadi, A. Al-Adhreai, A. Abdulwahab, *et al.*, "An investigation on the structural, morphological, optical, and antibacterial activity of sr: Cus nanostructures," Sci. Reports **14**, 25169 (2024).

[17] K. Raj, K. Sadaiyandi, A. Kennedy, and R. Thamizselvi, "Structural, optical, photoluminescence and photocatalytic assessment of sr-doped zno nanoparticles," Mater. Chem. Phys. **183**, 24–36 (2016).

[18] P. Ajibade and A. Oluwalana, "Enhanced photocatalytic degradation of ternary dyes by copper sulfide nanoparticles," Nanomaterials **11**, 2000 (2021).

[19] S. Aziz, A. Abdulwahab, and T. Aldeen, "Synthesis and characterization of (cdo-cuo-co3o4) mixed metal oxides nanocomposite," Sana'a Univ. J. Appl. Sci. Technol. **2**, 116–123 (2024).

[20] A. Abdulwahab, A.-A. A. Ahmed, A. Al-Hammadi, *et al.*, "Synthesis, characterization, and anti-cancer activity evaluation of ba-doped cus nanostructures synthesized by the co-precipitation method," RSC Adv. **15**, 4669–4680 (2025).

[21] M. Pal, N. Mathews, E. Sanchez-Mora, *et al.*, "Synthesis of cus nanoparticles by a wet chemical route and their photocatalytic activity," J. Nanoparticle Res. **17**, 1–12 (2015).

[22] S. Aziz, R. Abdulwahid, H. Rsaul, and H. Ahmed, "In situ synthesis of cus nanoparticle with a distinguishable spr peak in nir region," J. Mater. Sci. Mater. Electron. **27**, 4163–4171 (2016).

[23] M. Saranya, C. Santhosh, R. Ramachandran, *et al.*, "Hydrothermal growth of cus nanostructures and its photocatalytic properties," Powder Technol. **252**, 25–32 (2014).

[24] D. Pal, G. Singh, Y. Goswami, and V. Kumar, "Synthesis of randomly oriented self assembled cus nanorods by co-precipitation route," J. Mater. Sci. Mater. Electron. **30**, 15700–15704 (2019).

[25] K. Rajesh, P. Krishnan, A. Mani, *et al.*, "Physical strength and opto-electrical conductivity of l-serine phosphate single crystal for structural and photonics devices fabrication," Mater. Res. Innov. **24**, 295–300 (2020).

[26] A. Al-Sharabi, K. Sada'a, A. Al-Osta, and R. Abd-Shukor, "Structure, optical properties and antimicrobial activities of mgo–bi_2xcr_xo_3 nanocomposites prepared via solvent-deficient method," Sci. Reports **12**, 10647 (2022).

[27] D. Mamand, D. Muhammad, D. Muheddin, *et al.*, "Optical band gap modulation in functionalized chitosan biopolymer hybrids using absorption and derivative spectrum fitting methods: A spectroscopic analysis," Sci. Reports **15**, 3162 (2025).

[28] S. Khoreem and A. Al-Hammadi, "Studies on the electrical and optical conductivity of barium-nickel ferrite nanoparticles doped with zn," Discov. Nano **20**, 3 (2025).

[29] F. Hcini, M. Alzahrani, H. Hcini, *et al.*, "Structural, elastic, refractive index and energy band gap properties of li_0.5co_0.5fecro_4 ferrite for non-linear optical and optoelectronic applications," Preprints (2025). Preprint.

[30] E. Al-Mahdi, A. Abdulwahab, A. Alnehia, *et al.*, "Characterization of zn-doped cuscn nano-powders synthesized via an in situ method for enhanced optical and structural properties," Results Chem. **14**, 102140 (2025).

[31] H. Abou-Elnour, M. Osman, M. Fadel, and A. Shakra, "Investigation of the optical properties for quaternary se60xge35ga5sbx (x= 0, 5, and 10) chalcogenide glass," Materials **15**, 6403 (2022).

[32] P. González-Larraza, T. López-Goerne, F. Padilla-Godínez, *et al.*, "Ic50 evaluation of platinum nanocatalysts for cancer treatment in fibroblast, hela, and du-145 cell lines," ACS Omega **5**, 25381–25389 (2020).

[33] J. Jeronsia, D. Raj, L. Joseph, *et al.*, "In vitro antibacterial and anticancer activity of copper oxide nanostructures in human breast cancer michigan cancer foundation-7 cells," J. Med. Sci. **36**, 145–151 (2016).

[34] K. Ahmed, A. Nagy, R. Brown, *et al.*, "Silver nanoparticles: Significance of physicochemical properties and assay interference on the interpretation of in vitro cytotoxicity studies," Toxicol. Vitro **38**, 179–192 (2017).

[35] A. Makkawi, N. Aysa, and F.-A. Gassim, "Anticancer activity of zinc oxide and zinc oxide/cadmium sulfide nanocomposites," Asian J. Pharm. Clin. Res. pp. 535–539 (2019).